Electronic Supplementary Material (ESI) for Physical Chemistry Chemical Physics.

Morphology characterization of dendrites on lithium metal electrodes by NMR spectroscopy Supplementary Information

Santiago Agustín Maldonado-Ochoa[1,2], Muriel Zampieri[1,2], Manuel Otero[1,2], and Fabián Vaca Chávez[1,2]

[1] *CONICET, Instituto de Física Enrique Gaviola (IFEG), Córdoba, Argentina*

[2] *Universidad Nacional de Córdoba, Facultad de Matemática, Astronomía, Física y Computación, Córdoba, Argentina*

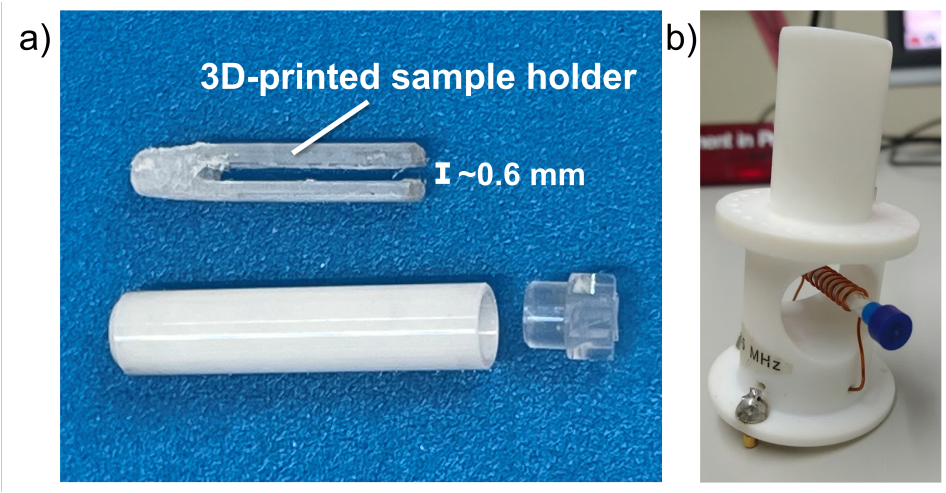

Figure S1: a) 3D-printed sample holder and NMR 4 mm zirconia rotor. b) NMR coil. The rotor is placed in a 5 mm diameter glass tube, which in turn fits in the solenoid.

Calculation of FID signal

The FID signals $S(t)$ were created by adding the signals from each voxel (indexed as α), with appropriate weighting w_α using the reciprocity principle , as shown in equation (2)[1]. To obtain the weights w_α, the resulting signals from each pulse sequence were calculated using the evolution of the density matrix $\hat{\rho}$. The initial state is described by the spin operator I_z. The evolution during the RF pulses is governed by the rotation operator P_1, represented by $\hat{\rho}_a = P_1 \hat{\rho}_b P_1^{-1}$, where $\hat{\rho}_b$ and $\hat{\rho}_a$ are the density matrices before and after the pulse, respectively. The evolution between pulses is influenced by longitudinal and transversal relaxation, with the diagonal elements of $\hat{\rho}$ relaxing with $T_1 = 170$ ms and off-diagonal elements with $T_2 = 600$ μs[2]. As the RF field B_1 is not uniform inside the metallic sample due to the skin effect, the rotation operator P_1 depends on the depth of the observed spin. The amplitude and phase of the RF field are described by[3]

$$B_1 = B_{1,0} \exp(-r/d) \exp(ir/d),$$

where d is the skin depth, r is the distance from the surface to the spin, and $B_{1,0}$ is the amplitude of the B_1 field at the surface. The skin depth is given by[4]

$$d = \sqrt{\frac{\rho_{\mathrm{Li}}}{\pi \mu_0 \mu_r f}},$$

where $\mu_0 = 4\pi 10^{-7}\,\mathrm{m\,kg\,A^{-2}\,s^{-2}}$ is the permeability of the vacuum, $\mu_r = 1 + \chi = 1.000024$ and $\rho_{\mathrm{Li}} = 92.8\,\mathrm{n\Omega\,m}$ are the relative permeability and the resistivity of metallic lithium[5,6], and f is the frequency of the applied RF field. In this study, a 7 T magnetic field was assumed, corresponding to a Larmor frequency of 116.6 MHz for ^{7}Li, yielding a skin depth of $d = 14\,\mu$m.

If the RF field is aligned with the x-direction of the rotating frame, the rotation operator P_1 is given by[3]:

$$P_1 = \exp\left[-i\phi_0 \exp(-r/d)\right] \exp\left[I_x \cos(r/d) + I_y \sin(r/d)\right],$$

where I_x and I_y are spin operator components and $\phi_0 = \gamma B_{1,0} t_p$ is the flip angle of the surface spins, with t_p the pulse duration.

After the evolution during the pulse sequence, the expectation values are calculated using $\langle I_{x,y} \rangle = \mathrm{Tr}\left[\hat{\rho} I_{x,y}\right]$. According to the reciprocity principle, the dependence of B_1 with depth also influences the detected signals. The signals obtained from depth r are described by[3]:

$$\langle I_x^{\mathrm{obs}} \rangle = \exp(-r/d)\left[\langle I_x \rangle \cos(r/d) - \langle I_y \rangle \sin(r/d)\right]$$
$$\langle I_y^{\mathrm{obs}} \rangle = \exp(-r/d)\left[\langle I_x \rangle \sin(r/d) + \langle I_y \rangle \cos(r/d)\right]$$

Finally, the weights are given by:

$$\mathrm{w}_\alpha(r) = \langle I_x^{\mathrm{obs}}(r) \rangle + i \langle I_y^{\mathrm{obs}}(r) \rangle$$

Notice that w_α are depth-dependent due to the skin effect, and also pulse sequence-dependent given that $\langle I_{x,y} \rangle$ depend on the evolution of $\hat{\rho}$ through the different rotation operations.

Microstructures shapes

Throughout this work, different shapes of microstructures have been used, varying the geometries and within them, the parameters height, radius and density. The different microstructures, shapes and their corresponding NMR SP sequence spectra are shown in the figure S2.

Sources of error

The main sources of error for the numerical calculations were identified as: radiofrequency field (RF) perurbations, edge effects, and discretization of the geometry.

RF field perturbations: The RF was assumed to be uniform over the material surface, and to decay exponentially in the direction perpendicular to the surface (implemented using the *erosion* operation from the morphological image processing technique). Conversely, Illot et al. demonstrated disruption of the RF field in the surroundings of Li microstructures by solving Maxwell's equations in 3D using the finite elements method[7]. Although this disruption suggests that the uniformity assumption appears not to be valid, it is expected that any change in the RF field at the surface would influence the excited regions, subsequently affecting the signal magnitudes. Our work primarily focuses on the perturbation of the static field, which remains unaffected by RF perturbations.

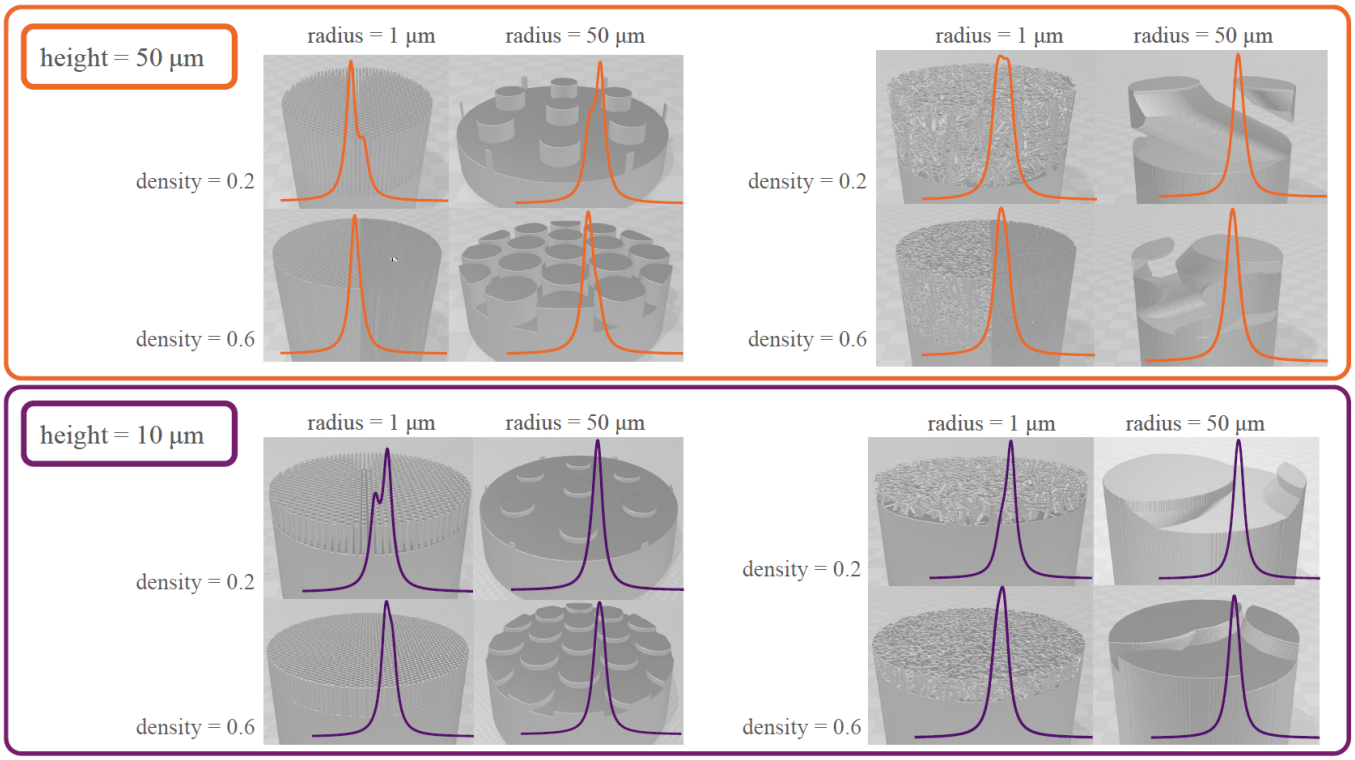

Figure S2: Microstructures shapes with their corresponding NMR spectra. The employed geometries are Hex/0° at the left and Rand/(14° to 76°) at the right.

Therefore, we can reasonably assume that the impact of RF field perturbations on the NMR spectrum is negligible.

Edge effects: It was observed that the microstructures in the edge region exhibit a higher $\Delta\delta$ shift compared to their center counterparts. This is because these microstructures sense a different environment, with a lower local density. In order to avoid these effects when studying the $\Delta\delta$ shifts as a function of density, a lateral superposition was implemented. The microstructures were simulated within a region that is approximately half of the FOV in each dimension. Once the magnetic field perturbation is calculated, it is spatially shifted and superimposed to create a region with an area 4 times greater. To illustrate the results of this method, Figure S3 shows the simulation of a hexagonal array of cylinders with height 10 μm, radius 5 μm, and density 0.4; without (S3a) and with (S3b) lateral superposition. The figures show a slice in the xy plane at half the cylinders' height. It is clear that the edge effect gives an error of several ppm, as can be seen in S3a. This error is minimized when the superposition is implemented, resulting in a more homogeneous $\Delta\delta$ among cylinders.

Discretization of the geometry: The number of voxels used to represent the cylinders, yields to errors not only in the representation of the microstructures shape, but also in the calculated magnetic field perturbation. This is strongly related to the inherent error of the method, as shown by Salomir et al.[8] and Bouwman et al.[9]. In both works, it can be observed that the larger error is found in the edges of the material. In order to evaluate the contribution of this kind of errors for our particular geometry sizes, a 1 μm radius metallic Li sphere immersed in a uniform static field B_0 (along the z-axis) was simulated with different voxel lengths and compared with the exact solution. Figure S4 shows the simulation of the magnetic field for the spheres with voxel lengths 0.125 μm, 0.25 μm, 0.5 μm, and 1 μm, which gives 16, 8, 4, and 2 voxels for representing the diameter, respectively. For 0.5 μm and 1 μm voxel lengths, the spheric characteristic of the object is clearly lost (S4a). The perturbation of the (macroscopic) magnetic field, $(B_{\text{mac}} - B_0)/B_0$, is shown in units of ppm in Figure S4b. Similar characteristics of the perturbation are observed despite the clear

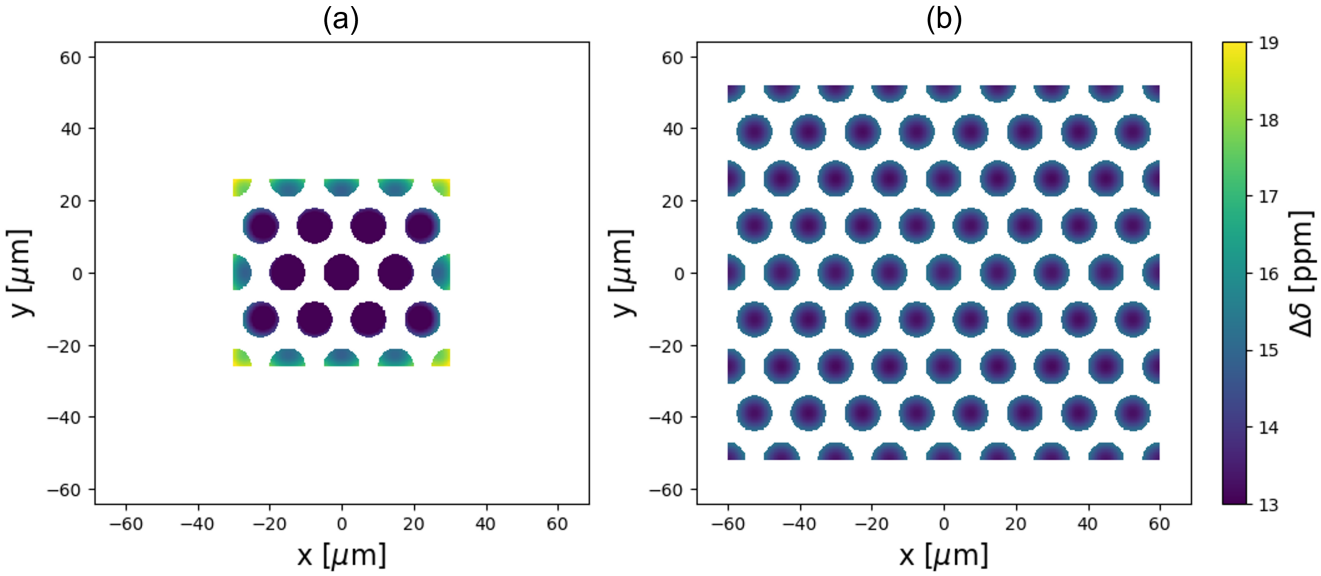

Figure S3: Simulation of a hexagonal array of cylinders with height 10 μm, radius 5 μm, and density 0.4. The slice is taken at half the cylinder's height. a) No lateral superposition, and b) with lateral superposition.

distinctions between the objects.

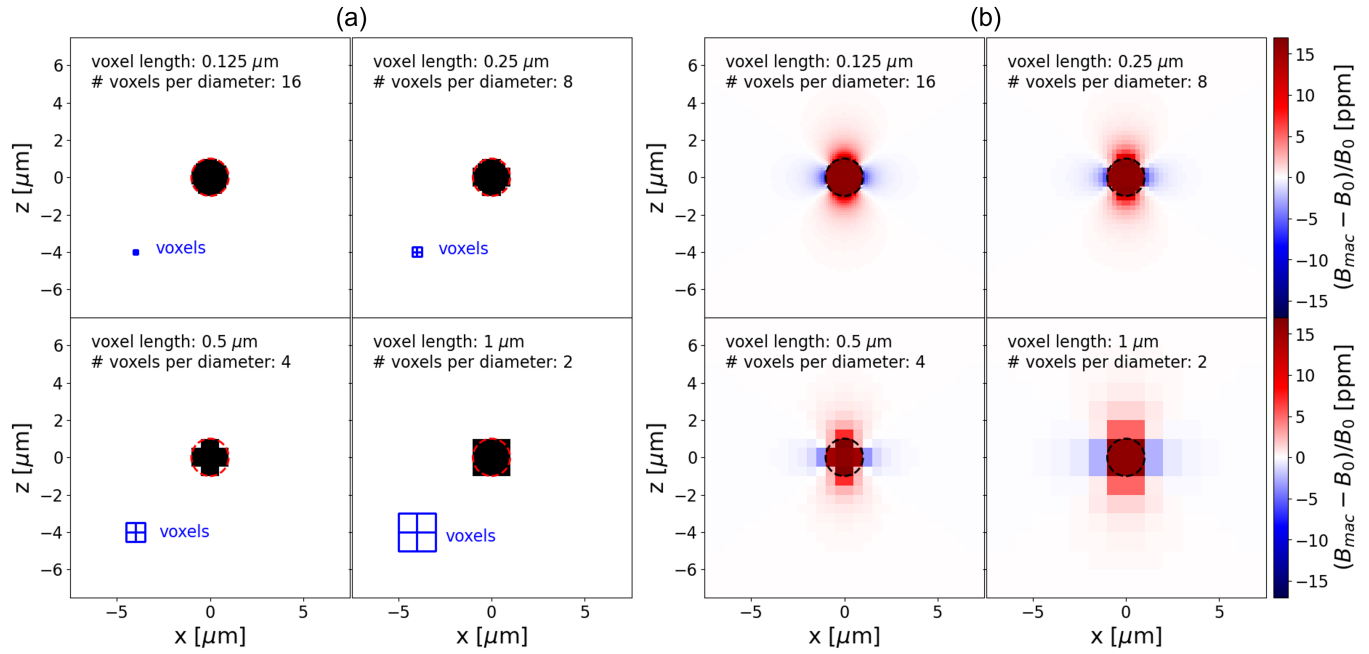

Figure S4: a) Discretization of a 1 μm radius sphere with voxel lengths 0.125 μm, 0.25 μm, 0.5 μm, and 1 μm. Four voxels are displayed for size comparison (blue). The red dotted lines indicate the exact sphere. b) Simulation of the perturbation of the z-component of the macroscopic magnetic field for different voxel lengths. The dotted lines indicate the sphere.

The numerical calculation of the field (B_{Numeric}) and the excact solution (B_{Exact}) were compared by evaluating both solutions along the z-axis (at $x = y = 0$) and the x-axis (at $y = z = 0$). Figure S5a shows such comparison along the z-axis. For most cases, while the exact solution is uniform within the sphere, the numerical solution is overestimated in the edges. The error along the

z-axis, $(B_{\text{Numeric}} - B_{\text{Exact}})/B_0$ in units of ppm, is shown in Figure S5b. While the larger voxel lengths exhibit errors as high as 2.5 ppm, for 16 and 8 voxels per diameter, an error of ± 0.5 ppm can be assumed.

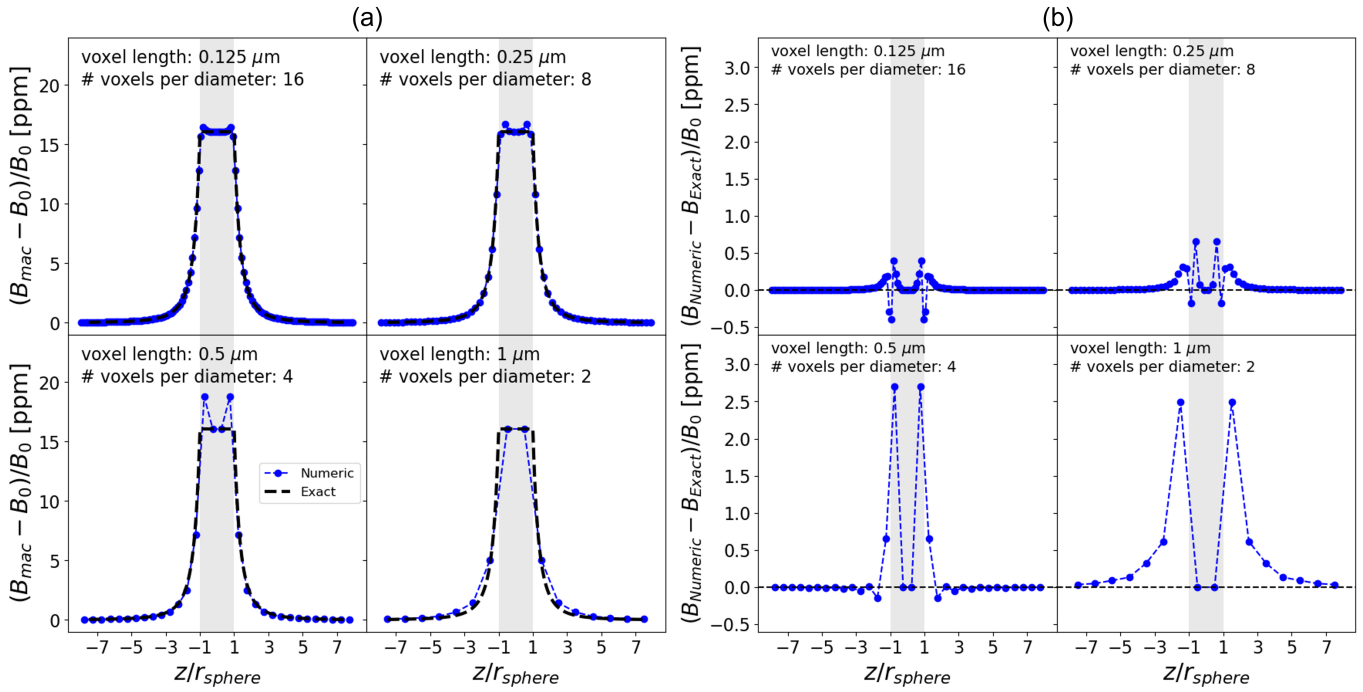

Figure S5: a) Comparison of the numerical and exact solution for perturbation of the z-component of the macroscopic magnetic field for different voxel lengths, along the z-axis. b) Error of the numeric solution along the z-axis. The grey strips represent the z-positions within the sphere.

The comparison between solutions and the error of the calculated magnetic field along the x-axis are shown in Figures S6a and S6b, respectively. Similar to the observations along the z-axis, the larger errors are found in the edges of the object. In addition, the errors are more pronounced for larger voxel lengths, as can be seen in S6b.

It is important to notice that the edge region is crucial, since it is the main contributor to the NMR signal (due to skin effect). Hence, the number of voxels used to represent the cylinders should be small enough to minimize the error of the method, but large enough to simulate a FOV including several cylinders. In this work, the smaller cylinders where simulated with radius 1 μm and 0.25 μm voxel length. Therefore an error of at least ± 0.5 ppm should be expected in the NMR spectra.

Spectra relative amplitude

The relative amplitude is defined by $A_{\text{mic}}/A_{\text{bulk}}$, where A_{mic} and A_{bulk} represent the integrals of the microstructures and bulk spectra, respectively. Fig. S7 depicts the relative amplitudes as a function of the density of cylinder-shaped microstructures.

It is important to note that the reported values correspond to a lithium surface region covered with different densities of microstructures. In real samples, the relative amplitude values are typically smaller due to contributions from regions without microstructures.

Construction of the Rand/(14° to 76°) geometry

The Rand/(14° to 76°) geometry involves cylinders that change their orientations, adapting random angles (θ_0, θ_1, θ_2) with respect to the z-direction and deviating at random angles (φ_0, φ_1, φ_2) with

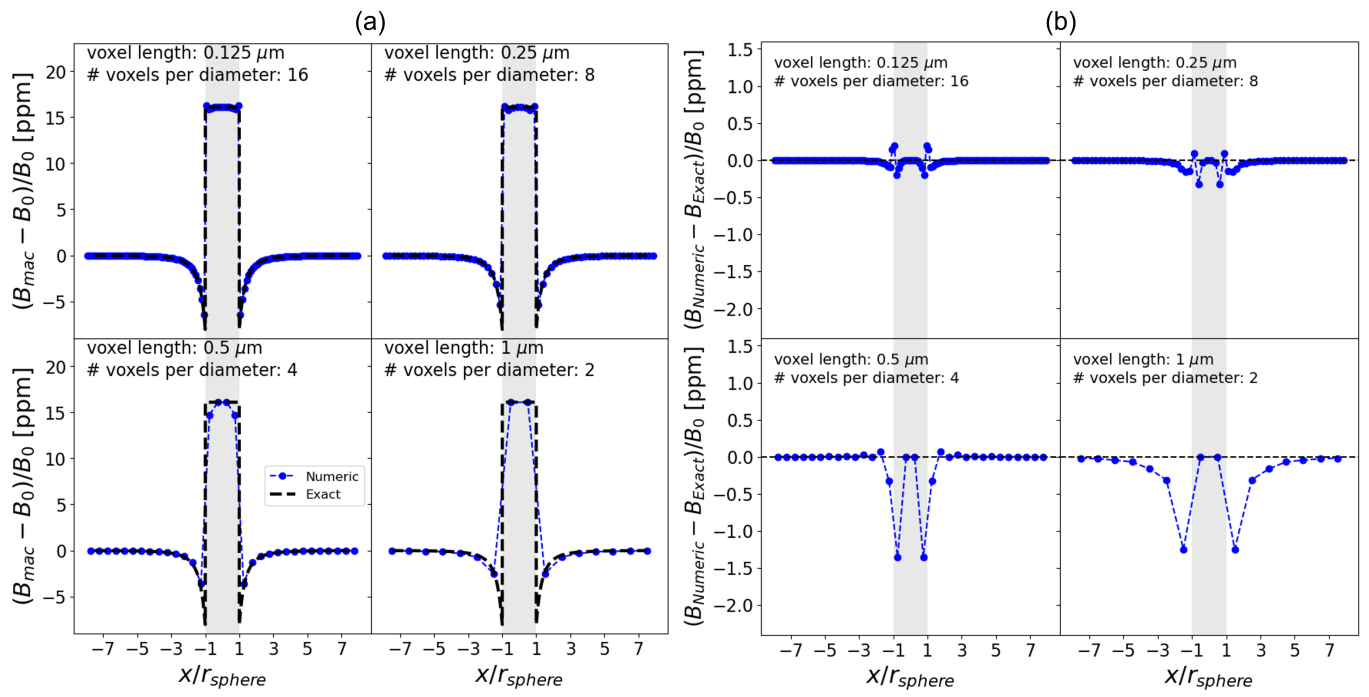

Figure S6: a) Comparison of the numerical and exact solution for perturbation of the z-component of the macroscopic magnetic field for different voxel lengths, along the x-axis. b) Error of the numeric solution along the x-axis. The grey strips represent the x-positions within the sphere.

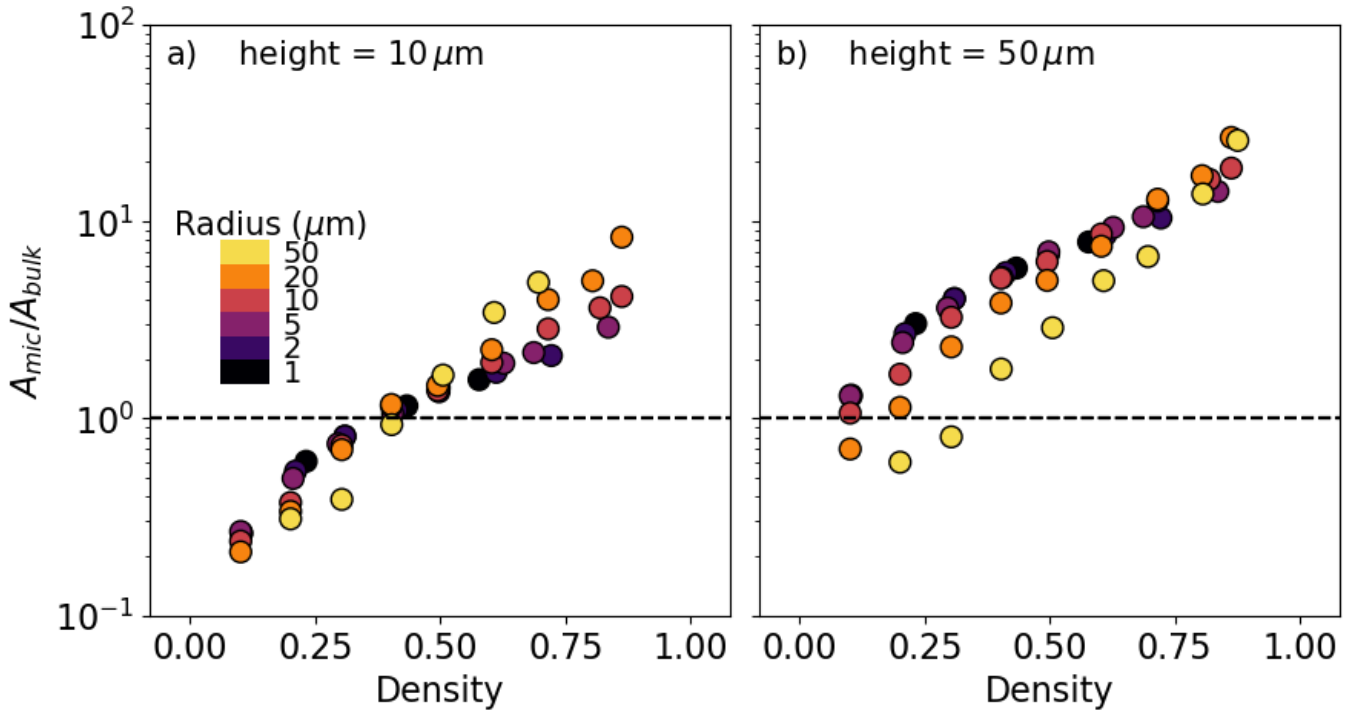

Figure S7: Relative signal amplitude of microstructures respect to bulk.

respect to the x-direction. Angle changes occur at two random z positions: the cylinders start with angles (φ_0, θ_0) at $z = 0$, then adopt angles (φ_1, θ_1) at z_1, and finally (φ_2, θ_2) at z_2, extending to a height h, as depicted in Fig. S8.

Since the cylinder is composed of stacked disks, the θ angle is determined by shifting the center of the disk as z increases. The direction of this shift is determined by φ, with n_z representing the

number of centered stacked disks and n_{xy} representing the number of voxels shifted. The resulting discrete angle is given by

$$\theta = \arctan \frac{n_{xy}}{n_z}.$$

In this study, we used ratios of n_{xy}/n_z such as 1/4, 1/3, 1/2, 1, 2, 3, and 4, resulting in angles of approximately 14°, 18°, 27°, 45°, 63°, 72°, and 76°, respectively.

Deviation was permitted in the $\pm x$, $\pm y$, or $\pm x \pm y$ directions, allowing φ to take values such as 0°, 45°, 90°, 135°, 180°, 225°, 270°, and 315°.

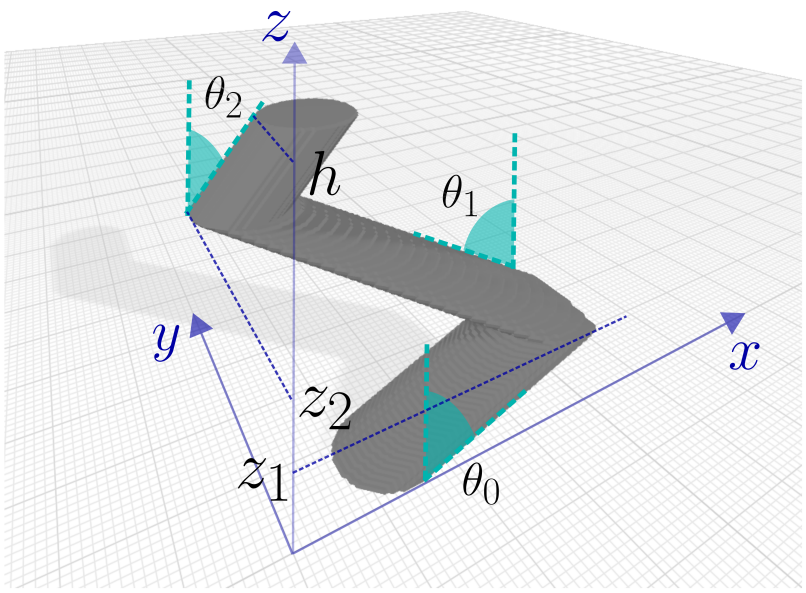

Figure S8: Scheme of a microstructure with the Rand/(14° to 76°) geometry.

References

[1] A. J. Ilott and A. Jerschow, Concepts in Magnetic Resonance Part A, 2018, **47A**, e21466.

[2] A. J. Ilott and A. Jerschow, Sci. Rep., 2017, **7**, 5425.

[3] M. Mehring, D. Kotzur and O. Kanert, Phys. Status Solidi B, 1972, **53**, K25–K28.

[4] R. Bhattacharyya, B. Key, H. Chen, A. S. Best, A. F. Hollenkamp and C. P. Grey, Nat. Mater., 2010, **9**, 504–510.

[5] W. Haynes, CRC Handbook of Chemistry and Physics, CRC Press, 2016.

[6] A. J. Ilott, S. Chandrashekar, A. Klöckner, H. J. Chang, N. M. Trease, C. P. Grey, L. Greengard and A. Jerschow, J. Magn. Reson., 2014, **245**, 143–149.

[7] A. J. Ilott, M. Mohammadi, H. J. Chang, C. P. Grey and A. Jerschow, PNAS, 2016, **113**, 10779–10784.

[8] R. Salomir, B. D. de Senneville and C. T. Moonen, Concepts Magn. Reson. Part B, 2003, **19B**, 26–34.

[9] J. G. Bouwman and C. J. G. Bakker, Magn. Reson. Med., 2012, **68**, 621–630.